A Hybrid Energy Model for Region Based Curve Evolution - Application to CTA Coronary Segmentation

Muhammad Moazzam Jawaid[a,*], Ronak Rajani[c], Panos Liatsis[b], Constantino Carlos Reyes-Aldasoro[a], Greg Slabaugh[a]

[a] *City, University of London, Northampton square, London, EC1V 0HB*
[b] *The Petroleum Institute, P.O.Box 2533, Abu Dhabi, UAE*
[c] *St Thomas' Hospital, Westminster Bridge Road, London, SE1 7EH*

Abstract

Background and Objective: State-of-the-art medical imaging techniques have enabled non-invasive imaging of the internal organs. However, high volumes of imaging data make manual interpretation and delineation of abnormalities cumbersome for clinicians. These challenges have driven intensive research into efficient medical image segmentation. In this work, we propose a hybrid region-based energy formulation for effective segmentation in computed tomography angiography (CTA) imagery.

Methods: The proposed hybrid energy couples an intensity-based local term with an efficient discontinuity-based global model of the image for optimal segmentation. The segmentation is achieved using a level set formulation due to the computational robustness. After validating the statistical significance of the hybrid energy, we applied the proposed model to solve an important clinical problem of 3D coronary segmentation. An improved seed detection method is used to initialize the level set evolution. Moreover, we employed an auto-correction feature that captures the emerging peripheries during the curve evolution for completeness of the coronary tree.

Results: We evaluated the segmentation accuracy of the proposed energy model against the existing techniques in two stages. Qualitative and quantitative re-

*Corresponding author
Email address: muhammad.jawaid.2@city.ac.uk (Muhammad Moazzam Jawaid)

sults demonstrate the effectiveness of the proposed framework with a consistent mean sensitivity and specificity measures of 80% across the CTA data. Moreover, a high degree of agreement with respect to the inter-observer differences justifies the generalization of the proposed method.

Conclusions: The proposed method is effective to segment the coronary tree from the CTA volume based on hybrid image based energy, which can improve the clinicians ability to detect arterial abnormalities.

Keywords: computed tomography images; coronary segmentation; hybrid image energy; level set method.

---

1. Introduction

Coronary artery disease (CAD, also known as atherosclerosis) relates to the accumulation of cholesterol and fatty materials inside coronary arteries. Its growth leads to an obstruction of the vasculature that supplies blood to the heart musculature. As a result, the heart muscles become oxygen starved which may result in fatal cardiac consequences including angina, heart failure and arrhythmias. The mortality rate of CAD has dramatically increased in the last decade around the globe. According to the fact sheet of the World Health Organization [1], CAD was the prevailing cause of death globally in 2013, resulting in 8.14 million deaths (16.8%) compared to 5.74 million deaths (12%) in 1990. Moreover, recent statistics of the National Health Services, United Kingdom [2] reveal that over 2.3 million people in the United Kingdom suffer from CAD where the annual death toll is approximately 73,000 (an average of one death every seven minutes). These substantial levels of ongoing morbidity and mortality have led to heightened interest in new methods to identify coronary abnormalities.

From a clinical point of view, the early detection of arterial abnormalities is crucial as future cardiac events can be avoided or at least delayed, by addressing the behavioural risk factors such as tobacco use, unhealthy diet and the physical routine. The conventional methods used to detect CAD include

catheter guided techniques X-ray angiography, optical coherence tomography (OCT) and intra-vascular ultrasound (IVUS); however, the invasive nature make these methods time consuming and sensitive as a considerable risk is involved. Moreover, the 2D angiogram-based representation of 3D vessels provides insufficient information to rule out the possibility of CAD as remodelling is often missed. In contrast, the recent advancements in non-invasive imaging have revolutionized the diagnostic accuracy as modern equipment has the potential to image sub-millimetre details of internal organs [3]. Especially, CTA has emerged as an important technique based on the fact that the internal organs can be well differentiated on the basis of intensity response. For example, in a cardiac CTA, the blood filled vessels appear comparatively brighter than the surrounding tissues, which facilitates manual tracking of the coronary structures with a reasonable accuracy. A shortcoming of the non-invasive imaging is the high volume of imaging data, where it becomes cumbersome for the clinicians to manually track structural abnormalities. Moreover, the manual analysis becomes time consuming and the diagnostic accuracy depends upon the previous knowledge and expertise of the radiologist. These limitations have driven an intensive research for automated diagnosis methods. The first step towards an effective diagnosis is segmentation of the anatomical object of interest from the background. Segmentation algorithms generally employ the intensity characteristics to split an image into n distinct regions. A simple criterion is the gradient strength which measures the directional change in the intensity of the image; however, gradient based methods result in erroneous segmentation in the absence of sharp distinctive boundaries. In contrast, region based segmentation methods exploit the principle of region homogeneity inside the image. Objects are classified in the image based on the assumption that neighbouring pixels constitute a homogeneous region if they have similar intensity. Region based methods have proven to be more robust for medical imagery, as they are less dependent on the initialization and more resistant to image noise [4]. Depending upon the complexity of the structures, a combination of features (geometric shape, texture, intensity) can be used for effective delineation of objects.

We now briefly summarize the flow of this paper. In Section 2, we review the literature related with the current work. Starting with the generic image segmentation, we conclude Section 2 with a focus on CTA coronary segmentation. Section 3 gives a general description of the CTA data in this work, whereas the proposed model is explained in Section 4. In Section 5, we compare the performance of proposed model with the existing segmentation methods. In Section 6, we provide the discussion and some future directions for this work.

2. Related Work

Active contours have been a popular choice for image segmentation in recent years [5]. The motivation for the active contour model is the seminal work of Kass *et al.* [6] in which the object segmentation was posed as an energy minimization problem. According to this model, the object boundaries can be captured in an image with the help of a parameterized evolving contour where the evolution of the moving contour is regulated by a complex energy metric as expressed in Eq. 1.

$$E = \int_0^1 E_{int}\left(C_s\right) + E_{ext}\left(C_s\right) + E_{cons}\left(C_s\right) ds \tag{1}$$

where C_s denotes the evolving curve parameterized by s, and s is the curve arc-length. The internal energy E_{int} penalizes the bending and stretching of the curve to ensure smoothness, E_{ext} represents image based energy (intensity statistics) and E_{con} refers to explicit constraints imposed by the user. Caselles *et al.* [7, 8] proposed the geometric contour models to address the topological changes during evolution. In contrast to the parametric representation of Kass *et al.* [6], the geometric model was based on the level set formulation [9] which allows the tracking of complex moving structures.

Apart from the contour representation, the curve driving force E_{ext} plays a decisive role in the successful delineation. Methods reported in [6, 7, 8, 10] approximated the image energy E_{ext} in terms of gradient strength, whereas Chan and Vese [4] and Yezzi *et al.* [11] reported the use of region based statistics.

Based on the assumption of homogeneous intensity for the object and background region, Chan-Vese approximated two regions with their global mean intensities. Similarly, the energy formulation of Yezzi *et al.* [11] employed the idea of maximal separation between two mean intensities of a piecewise constant image. Consequently, the optimal segmentation can be achieved for both models when the evolving curve captures the boundary of the object. Likewise, an effective use of the level set based evolution is recently reported by Wang *et al.* [12] for CTA based liver segmentation. Accordingly, the authors integrated shape-intensity joint prior constraints in Chan-Vese energy formulation for accurate segmentation of liver in CTA volume.

It should be noted that the global approximation of image statistics lead to a good segmentation in generic images but fails to handle complex medical data [13], as medical images often violates the piecewise constant assumption. Intensity inhomogeneity often occurs in medical images due to the acquisition hardware artefacts, partial volume effect and different types of noise. In other cases, it also appears due to the nature of data i.e. the non-uniformity of tissues leads to an increased inhomogeneity [14]. An effective way to overcome the inhomogeneity problem is to approximate the image based energy E_{ext} using a fairly small region, so that curve evolves according to the local intensity distribution. The incorporation of localized statistics in the image segmentation was first proposed by Brox and Cremers in [15], where the piecewise smooth model of Mumford-Shah [16] was approximated by the local means. Similarly, Xu *et al.* [17] proposed the use of local intensity statistics in a hybrid model for an improved segmentation. Accordingly, the authors used global approximation in Chan-Vese energy model and the local approximation in the mean separation energy model of [11]. An improved segmentation was achieved by using a weighted contribution of two terms; however, the computational cost increases in terms of a two-fold segmentation. Moreover, the method was quantitatively evaluated only on 2D images and no results were reported for complex 3D multi-scale images. Lankton and Tannenbaum [18] proposed a novel method for localized region based segmentation by introducing a radius-based

kernel to define the localization scope. Successful results were presented for both 2D image segmentation [18] and 3D coronary segmentation [19]; however, the initialization sensitivity was explicitly emphasized. We have observed from experimentation that the selection of the localization radius is critical in this method. A large radius leads to a global approximation resulting in erroneous segmentation, whereas a small radius makes the evolving contour vulnerable to spurious local minima. Another limitation of this method is the demand for intelligent placement of the initial mask to avoid the local optima problem.

In context of the vessel segmentation, Cheng *et. al.* [20] proposed a novel idea of 2D cross-section based boundary detection of 3D vessels. According to the proposed method, the vessel axis was computed in the first stage using multi-scale Hessian analysis. In the following step, a active contour model was evolved to detect the vessel boundaries under shape and size constraints for improved accuracy; however, the main limitation of the method is circular shape approximation of the vessels. Consequently, the pathological lesions and vessel morphological abnormalities may lead to inaccurate segmentation in this method. Yang *et al.* [21] reported an edge-based method for the segmentation of coronary tree from the CTA volumes. The authors employed an adaptive inflation principle that allowed the bidirectional growth of the evolving curve based on the curve position. A two class Gaussian Mixture Model was approximated from the image histogram to obtain the edge map of the CTA volume; however, a violation of two class behaviour in CTA volume may lead to the erroneous segmentation as curve evolution is fully dependent on the resultant edge map. Yin and Liatsis [22] proposed a hybrid energy model by integrating the global image behaviour in the coronary evolution. In a pre-processing stage, voxels representing the air in the CTA volume were normalized to obtain a two class representation. Next, using the assumption of a constant background, a bimodal histogram was approximated with a Gaussian Mixture Model. In the final stage, an explicit label image was derived using a cumulative distribution function of the histogram to represent the global model of the CTA image. This method works efficiently for the bimodal images; however, it fails to handle

the significant variations in CTA data encountered in practice. For instance, the intensity shift in the background makes this approach vulnerable as the label image misguides the evolving contour. Another limitation is the exclusive pre-processing required for individual volumes as the acquisition dependent parameters affect the quality of the CTA differently.

We make two basic contributions in this work. First, we introduce a hybrid energy formulation that integrates the local intensity and a probability based global discontinuity map of the image. The proposed hybrid energy based model captures object boundaries accurately as the hybrid energy is less attracted to the local optima solutions. Moreover, the hybrid energy provides robustness against the initialization and localization radius simultaneously, as demonstrated in Section 5. The second contribution is the application of the proposed energy model to solve an important clinical problem of coronary segmentation. In the first stage, coronary seed points are detected based on Han *et al.'s* [23] method; however, we reduced the false positive detections by imposing a contrast medium based intensity constraint. In addition, we introduced an auto-correction feature for the mask, which captures the emerging peripheries during the evolution process. The superiority of the proposed model is illustrated by comparing the segmentation performance against coronary segmentation model of Yang *et al.* [21].

3. Clinical CTA Data

In this work we used the clinical CTA data of the Rotterdam coronary artery algorithm evaluation framework [24, 25]. The Rotterdam CTA data comes from different institutions and is based on different vendors as illustrated in Table 1. This multi-vendor data makes the coronary segmentation challenging; however, it serves as a great platform to ensure the generalization of the proposed algorithm. We investigated a total of 18 CTA volumes, for which the lumen segmentation ground truth is also provided. The segment-wise [26] reference ground truth is provided in terms of 3D discrete contours defining the lumen

boundary along the length of the segment.

Table 1: CTA data used in coronary segmentation.

Vendor	Siemens	Toshiba	Philips
Volume Count	6	6	6
Institution	Erasmus MC Uni. (NL)	Leiden Uni. (NL)	Utrecht Uni. (NL)
CT Scanner	Somatom Def.	Aquilion One 320	Brilliance 64
Slice/Rotation	32x2	320x1	64x1
ECG Gating	Retrospective	Retrospective	Retrospective
Reconstruction Kernel	b26f	b26f	b26f
Contrast Medium	Ultravist 370	Ultravist	Ultravist 370

It should be mentioned that the main theme of the Rotterdam framework is stenosis grading in the coronary tree; however, the provision of the manual ground truth for lumen makes this data suitable for coronary segmentation problems.

4. Proposed Model

In this work, we propose to integrate the discontinuity map (global model) in the localized segmentation of Lankton *et al.* [18] for an improved accuracy. The localized model computes the image based energy E_{ext} from a radius constrained region, which often leads to the local optima problem. Thus, it demands a careful initialization for the desired segmentation, which is not always straightforward in the case of complex medical structures. In contrast, the integration of the image global model in the curve evolution process will allow a certain amount of flexibility in the placement of initial contour. In case of far initialization, the global term will push the contour towards the object boundary by suppressing the influence of local optima. Moreover, a scalar weight regulates the influence of the global term to achieve a desired segmentation. A higher weight of the global term will push contour rapidly towards the salient

features, whereas a lower weight will allow the localized statistics to fine tune the object boundaries. Accordingly, we will show that the hybrid energy based curve evolution will make the segmentation process robust i.e. less sensitive to the initial placement of the mask and more flexible against the localization scale. For the rest of the paper, we let I denote an image (3D CTA volume) defined on the domain Ω. Moreover, C represents a closed contour to be evolved and $\mathbf{x}$, $\mathbf{y}$ denotes two independent spatial variables such that each represent a point in the domain Ω.

4.1. Contrast Medium Approximation

A contrast medium is injected intravenously for enhanced visualization of blood-filled coronaries as a part of the CTA examination; however, the diffusion is not homogeneous in all patients. Consequently, we start with the assumption that the mathematical modelling for the contrast medium behaviour in an individual CTA volume may lead to an improved segmentation of the coronary tree. Since the blood flows into coronaries from the descending aorta, we therefore segmented the aorta in the first step to investigate the impact of contrast medium. The bright appearance of the aorta in Fig. 1c reflects the presence of the contrast medium. For aorta segmentation, we first applied an intensity threshold of 100 HU [27] to enhance the visualization of blood voxels (i.e. to suppress the lungs and soft tissues) as shown in Fig. 1b. Based on the circular appearance of the aorta in 2D axial planes, we applied a circular Hough Transform [28] based shape analysis in the subsequent step to segment the aorta from the blood volume as shown in Fig. 1c. Iteratively, 2D segmentation is performed through axial slices until the circular aorta changes shape which reflects the coronary origin. Next, we computed the intensity histogram of the segmented aorta and modelled the mean response of contrast medium with the help of a Gaussian distribution function. Fig. 1d shows the intensity distribution in the segmented aorta for three different volumes. A significant difference in the mean intensity value emphasizes the need of using contrast medium model in the segmentation process.

The Gaussian mean represents the intensity value for contrast filled blood in the descending aorta; however, the concentration of the contrast medium decreases as the blood flows away from the aorta to distal segments of the coronary tree. Moreover, the diffusion is also affected by the vessel remodelling and intermediate plaque instances which results in ambiguous appearance of distal segments. Thus, we accommodated the intensity drop by approximating it with twice the standard deviation as follows:

$$R_I = \{\mu_I \pm 2\sigma_I\} \tag{2}$$

where μ_I and σ_I represent the aorta based mean intensity and standard deviation for the respective CTA volume. The intensity range R_I establishes a realistic intensity interval for the coronary tree. We use the lower value to track the vessel progression towards the distal segments, whereas the upper threshold is used used to normalize the potential calcifications.

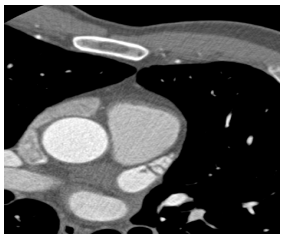

(a) 2D axial slice.

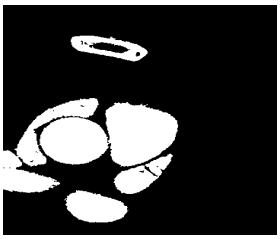

(b) Blood mask.

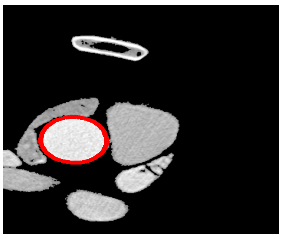

(c) Aorta segmentation.

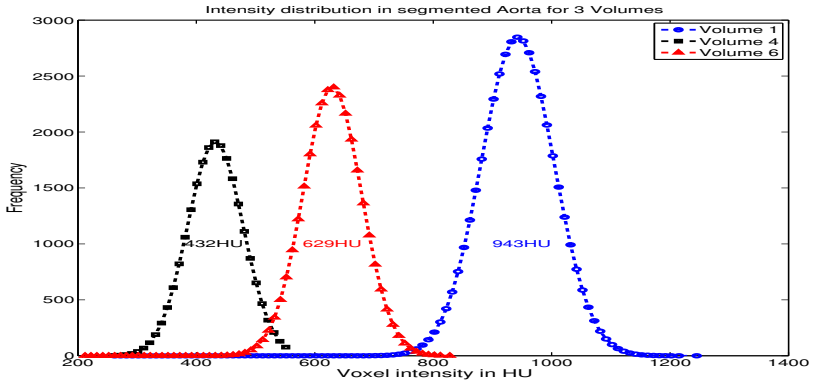

(d) Gaussian approximation for segmented aorta intensity distribution.

Figure 1: Contrast medium approximation in a CTA volume. (a) shows the 2D axial slice where contrast filled aorta is comparatively brighter. (b) and (c) shows the aorta segmentation using an intensity threshold of 100 HU and circular Hough transform. (d) shows the intensity distribution of segmented aorta for 3 CTA volumes, where a significant variation refers to contrast medium behaviour.

4.2. Coronary Seed Detection

Coronary seed points are required to initialize the region growing segmentation in the 3D CTA volume. For fast identification of the coronary seeds, we exploited the fact that the coronary arteries appear as tubular structures along the z dimension in the CTA volume. Consequently, we used Hessian based eigen value analysis to identify the local geometry in 3D CTA volume as proposed by Frangi *et al.* [29]. Accordingly, we computed the vesselness measure for the complete volume using Eq. 3.

$$V_o\left(\mathbf{x}\right) = \begin{cases} 0 & \text{if } \lambda_2 \ or \ \lambda_3 > 0 \\ \left\{1 - exp\left(-\frac{R_A^2}{2\alpha^2}\right) exp\left(-\frac{R_B^2}{2\eta^2}\right)\left(1 - exp\left(\frac{S^2}{-2\zeta^2}\right)\right)\right\} & \text{otherwise} \end{cases} \tag{3}$$

where term R_A and R_B discriminate the tubular structures from plate and blob patterns based on geometrical orientation and S serves as a penalty term to suppress the background noise. Moreover, $\lambda_1, \lambda_2, \lambda_3$ represents three eigen values and the α, η and ζ are the tuning parameters which are set equal to 0.5, 0.5 and 220 (i.e. the default values proposed in [29]). It should be noted that, to investigate the coronary at different scales in a CTA volume, a scale range of $[1-5]$ is used and $V_o(\mathbf{x})$ represents the maximum vesselness for voxel $\mathbf{x}$ obtained at the optimal scale. An inherent characteristic of the multi-scale vessel filter is the assignment of high vesselness measure to the object edges in the image. This is illustrated in Fig. 2a where the computed vesselness is plotted for a 2D axial image. To overcome this limitation, we employed a cylindrical filter [23] to further enhance the tubular structures in a CTA volume. Accordingly, the cylindrical filter is used to compute normalized local vesselness measure $V_c(\mathbf{x})$ using orthogonal cross sections such that *one* defines an ideal tubular structure and *zero* otherwise. In the subsequent step, response of the local cylindrical model was combined with the multi-scale vesselness to identify the potential coronary segments. To avoid erroneous seed detection, we used a threshold based classification to label the candidates voxels $\mathbf{x}$ according to Eq. 4.

$$s_o\left(\mathbf{x}\right) = \begin{cases} 1 & \text{if } V_o\left(\mathbf{x}\right) \geq T_f \ and \ V_c(\mathbf{x}) \geq T_{gf} \\ 0 & \text{otherwise} \end{cases} \tag{4}$$

where $s_o(\mathbf{x})$ denotes the seed label i.e. 1 denotes coronary seed and 0 otherwise. As proposed in [23] algorithm, we had chosen fairly small values for multi-scale vesselness $T_f = 10^{-3}$ and cylindrical response $T_{gf} = 10^{-4}$ thresholds to ensure that all potential tubular candidates are examined in the seed detection process.

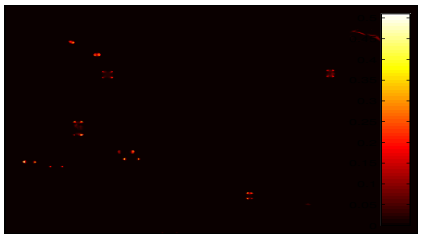

(a) vesselness measure for 2D slice.

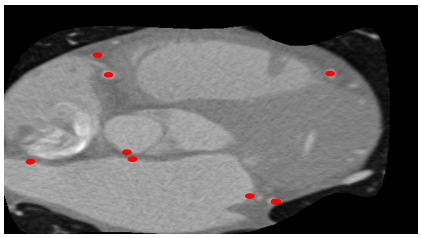

(b) Seed points using Han[23] method.

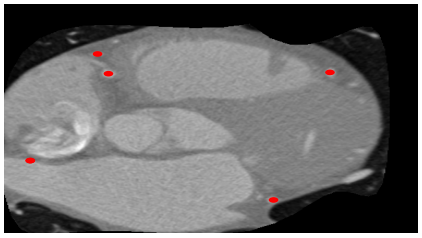

(c) Seed points using intensity constraint.

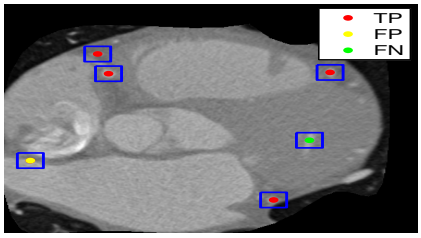

(d) Mask initialization in 6 mm neighbourhood.

Figure 2: Coronary seed detection and mask initialization. (a) show that the [29] model has assigned considerable vesselness for image edges. (b) represents the consequent seed points with numerous false positives. (c) and (d) show the improved seed points and the associated mask for initializing the region based segmentation. For best visualization of coloured images, refer to online version.

It can be observed from Fig. 2b that seed detection process based on Eq. 4 incurs a number of false positives. This is due to the fact that both geometrical filters had taken into account the shape features only. As a result, the elongated heart muscles and the surrounding non-coronary vasculature have been marked as the coronary segments which resulted in numerous false positive seeds. To suppress the non-coronary seed points, we posed our intensity based constraint in the seed detection process and redefine Eq. 4 to obtain improved seed label $s_o^{'}$ as follows:

$$s_o^{'}(\mathbf{x}) = \begin{cases} 1 & \text{if } V_o(\mathbf{x}) \geq T_f \ \textit{and} \ V_c(\mathbf{x}) \geq T_{gf} \ \textit{and} \ I(\mathbf{x}) \in R_I \\ 0 & \text{otherwise} \end{cases} \tag{5}$$

Equation 5 ensures that only those candidates seed points are retained in the

final set $s_o^{'}$ which satisfy the HU intensity criteria R_I of the respective CTA volume. Fig. 2c illustrates the efficacy of intensity based constraint R_I as the majority of the false positives has been eliminated. Next, we initialize a localized mask spanning over the region of 6 millimeters around the detected coronary seed points. A 6 mm neighbourhood is selected as the coronary segments are well encompassed within the mask area on the axial slice of a CTA image [30, 31, 32].

4.3. Hybrid Energy Approximation

4.3.1. Local Energy Modelling

We derive the local energy term in the first stage by using an extension of the Chan-Vese energy model. For an image I, the mathematical representation for the Chan-Vese algorithm is as follows:

$$F(c_1, c_2, C) = \int_{inside(C)} [I(\mathbf{x}) - c_1]^2 d\mathbf{x} + \int_{outside(C)} [I(\mathbf{x}) - c_2]^2 d\mathbf{x} + \gamma length(C) \tag{6}$$

where C is the evolving contour, c_1, c_2 represent the global mean intensity for two regions (i.e. inside and outside the curve) and γ is the regularization weight term to enforce contour smoothness. The optimal segmentation is achieved when the two regions are best approximated with their global mean values, as it leads to the minimal fitting error $F(c_1, c_2, C)$. For computational robustness, we redefine the Chan-Vese segmentation using level set formulation as expressed in Eq. 7. In the level set representation, the unknown curve C has been replaced with a signed distance function $\phi(\mathbf{x})$, such that the curve C is represented as zero level set $C = \{\mathbf{x} \mid \phi(\mathbf{x}) = 0\}$.

$$F(c_1, c_2, \phi) = \int_\Omega H\phi(\mathbf{x}) \left(I(\mathbf{x}) - c_1\right)^2 d\mathbf{x} + \int_\Omega (1 - H\phi(\mathbf{x})) \left(I(\mathbf{x}) - c_2\right)^2 d\mathbf{x} + \gamma \int_\Omega \delta\phi(\mathbf{x}) \left|\nabla\phi(\mathbf{x})\right| d\mathbf{x} \tag{7}$$

Based on the signed distance representation, we used the Heaviside function $H\phi(\mathbf{x})$ to select the interior of the curve C, whereas the exterior region is selected using the complementary equation $(1 - H\phi(\mathbf{x}))$. Moreover, the interface at the zero level set is obtained by using Dirac delta function $\delta(\phi)$. The $\delta(\phi)$ is the derivative of the $H(\phi)$, which is 1 when $\phi(\mathbf{x}) = 0$ and 0 far from the interface. The mathematical representation for the Heaviside and Dirac delta function is as follows:

$$H\phi(\mathbf{x}) = \begin{cases} 1, & \text{if } \phi(\mathbf{x}) \geq 0 \\ 0, & \text{if } \phi(\mathbf{x}) < 0 \end{cases}, \quad \delta\phi\left(\mathbf{x}\right) = \begin{cases} 1, & \text{if } \phi\left(\mathbf{x}\right) = 0 \\ 0, & \text{otherwise} \end{cases} \tag{8}$$

To address the intensity inhomogeneity problem of the CTA data, we employed the localization statistics in the energy minimization process as proposed by Lankton and Tannenbaum [18]. Accordingly, a radius based mask (6 mm in this work) is used to select the localized neighbours as expressed in Eq. 9. Accordingly, the selection kernel will be 1 when a spatial point $\mathbf{y}$ lies within a region of radius R_L centred at $\mathbf{x}$, and 0 otherwise.

$$B\left(\mathbf{x}, \mathbf{y}\right) = \begin{cases} 1, & \text{if } |\mathbf{x} - \mathbf{y}| < R_L \\ 0, & \text{otherwise} \end{cases} \tag{9}$$

The interaction of the localization kernel with the evolving curve is graphically illustrated in Fig. 3, whereas the mathematical model for computing the localized mean intensity inside and outside the curve (c_1, c_2 respectively) is expressed in Eq. 10.

$$c_1(\phi) = \frac{\int_{\Omega y} B(\mathbf{x}, \mathbf{y}) I(\mathbf{y}) H\phi(\mathbf{y}) d\mathbf{y}}{\int_{\Omega y} B(\mathbf{x}, \mathbf{y}) H\phi(\mathbf{y}) d\mathbf{y}}, \quad c_2(\phi) = \frac{\int_{\Omega \mathbf{y}} B(\mathbf{x}, \mathbf{y}) I(\mathbf{y}) (1 - H\phi(\mathbf{y})) d\mathbf{y}}{\int_{\Omega y} B(\mathbf{x}, \mathbf{y}) (1 - H\phi(\mathbf{y})) d\mathbf{y}} \tag{10}$$

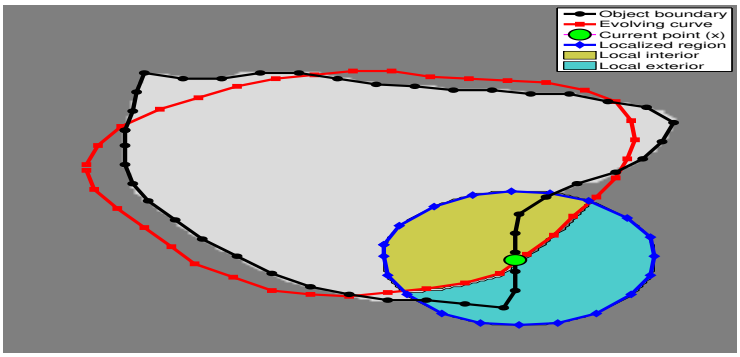

Figure 3: Kernel function for localized interior and exterior statistics. Red shows the evolving curve, whereas the blue represents the localized ball region $B(\mathbf{x}, \mathbf{y})$. For the current point (green), the localized interior and exterior are shown as yellow and cyan.

The minimization problem expressed in Eq. 7 can be solved using an Euler-Lagrange formulation as outlined in [4]. The subsequent application of the gradient descent method for optimal deformation leads to Eq. 11. For additional explanation and detailed derivation readers are referred to [4, 18].

$$\begin{aligned}\frac{\partial \phi}{\partial t}(\mathbf{x}) =& \delta\phi(\mathbf{x}) \int_{\Omega\ \mathbf{y}} \phi(\mathbf{y}) B(\mathbf{x}, \mathbf{y}) \left\{ (I(\mathbf{y}) - c_1)^2 - (I(\mathbf{y}) - c_2)^2 \right\} d\mathbf{y} \\ &+ \gamma \delta\phi(\mathbf{x}) div \left\{ \frac{\nabla\phi(\mathbf{x})}{|\nabla\phi(\mathbf{x})|} \right\} \end{aligned} \tag{11}$$

The image based force responsible for the curve evolution can be identified by discarding the regularization term of evolution Eq. 11. Accordingly, the localized curve driving force can be written as follows:

$$F_{local} = \delta\phi(\mathbf{x}) \int_{\Omega_{\mathbf{y}}} \phi(\mathbf{y}) B(\mathbf{x}, \mathbf{y}) \left\{ (I(\mathbf{y}) - c_1)^2 - (I(\mathbf{y}) - c_2)^2 \right\} d\mathbf{y} \tag{12}$$

The practical efficiency of F_{local} depends upon several factors including careful selection of the localization radius and the intelligent placement of the initial mask. The sensitivity to the initialization makes this method delicate as small perturbations in the initialization may lead to an undesirable solution. Fig. 4 presents two simple cases for synthetic images where the localized curve evolution fails to handle small perturbations in initial mask.

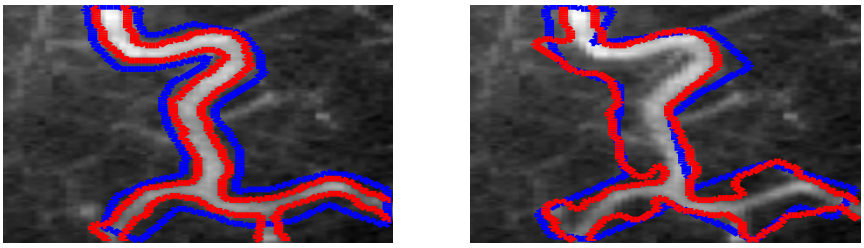

(a) Segmentation result for careful initialization.

(b) Perturbation leads to erroneous segmentation.

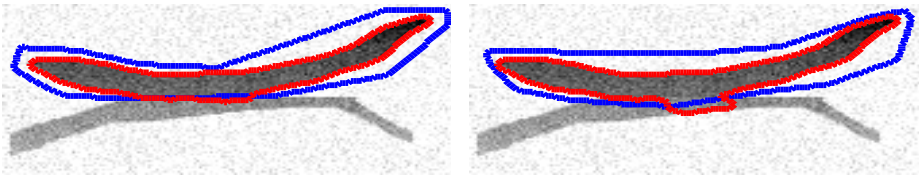

(c) Segmentation result for careful initialization.

(d) Perturbation leads to erroneous segmentation.

Figure 4: The sensitivity of the localization model against initial mask. (a) and (c) show the segmentation result for a cautious initialization, that is, very close to the manual delineation. On the other hand (b) and (d) show the result when perturbations are introduced in the initial mask. Blue is the initial mask and red is the final segmentation result.

To overcome this limitation, we propose to integrate the global model of the image in the segmentation process. Consequently, we redefine the curve driving force as expresed in Eq. 13.

$$F_{hybrid} = \{F_{local} + \beta F_{global}\} \tag{13}$$

where β is the constant weight regulating the influence of the global term for achieving the desired segmentation. The mathematical model for obtaining image based F_{global} is explained in the following section.

4.3.2. Global Energy Modelling

The global model of the image is derived by identifying the intensity discontinuities in image. Conventionally the gradient is used for defining an edge-map of an image; however, the gradient generally thickens the object boundary as shown in Fig. 5b. Thus, the quality of the segmentation is compromised as the evolving contour stops away from the true borders of the object. One possibility is the use of smaller gradient scale; however, the selection of the optimal scale directly influences the segmentation quality. In contrast, the Bayesian framework leads to sharp inter-class distinctions [21] inside an image as presented in Fig. 5c. This characteristic makes the Bayesian approach more feasible for the coronary segmentation problem as the cardiac CTA data is generally approximated using a three class assumption [13, 21, 22].

Based on clinical interpretation of the cardiac CTA, we start with the assumption that the histogram of the CTA volume can be well approximated using three classes (air filled lungs, heart tissues and the blood filled structures). However, we applied a precautionary normalization to suppress the calcifications (if any) in the CTA volume by clamping the intensity against the upper threshold value of the respective R_I intensity range. Next, we approximated the individual peaks of the image histogram to obtain the Gaussian approximation for three individual classes using Eq. 14.

$$p\left(I\left(\mathbf{x}\right) \mid \mathbf{x} \in c_k\right) = N\left(d, \mu_k, \sigma_k\right) = \frac{1}{\sigma_k\sqrt{2\pi}} exp^{\frac{-(d-\mu_k)^2}{2\sigma_k^2}} \tag{14}$$

where $d = I(\mathbf{x})$ denotes the intensity levels in the volume I at position $\mathbf{x}$, c_k is the class identifier and (μ_k, σ_k) represent distribution parameters of the respective class.

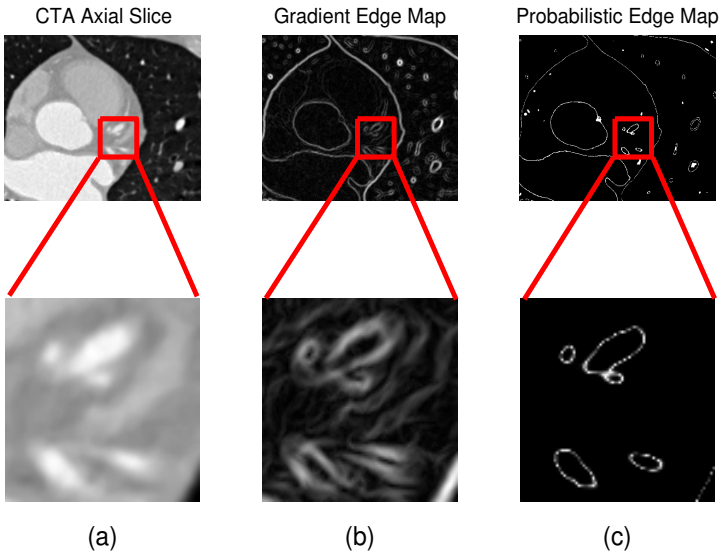

Figure 5: Image discontinuity modelling based on two methods. (a) shows the 2D axial slice with coronary segments. (b) shows the edge map obtained using gradient strength which leads to thicker edges. (c) presents shows the probabilistic difference based discontinuity map with sharp edges.

In the subsequent step, the overall histogram of the CTA is represented using a Gaussian mixture model where individual peaks are mapped to a weighted Gaussian distribution as expressed in Eq. 15.

$$p(d) = \sum_{k=1}^{3} a_k N(d; \mu_k, \sigma_k) \tag{15}$$

Next, the expectation maximization [33] algorithm is iteratively applied to determine the optimal distribution parameters for each class where the prior probability is set equivalent for all three classes at the start. In the final step, Bayes' rule is applied to obtain the voxel-wise posterior probabilities (i.e. probabilities of a single voxel $\mathbf{x}$ with intensity value d, for three different classes).

$$Pr(\mathbf{x} \in c_k \mid I(\mathbf{x}) = d) = \frac{Pr(I(\mathbf{x}) = d \mid \mathbf{x} \in c_k) Pr(\mathbf{x} \in c_k)}{\sum_{\tau=1}^{n} Pr(I(\mathbf{x}) = d \mid \mathbf{x} \in c_\tau) Pr(\mathbf{x} \in c_\tau)} \tag{16}$$

where $Pr(I(\mathbf{x})|c_k)$ and $Pr(\mathbf{x} \in c_k)$ represent the likelihood and the prior probability function for three individual classes. To minimize the impact of probabil-

ity approximations, we applied anisotropic diffusion as proposed by Perona and Malik [34]. A total of five iterations are applied to achieve smoothed posteriors Pr^{Smth} with gradient modulus (Kappa) set equal to 30. In the subsequent step, we derive the global model of the image as the squared difference of the two largest posteriors for every pixel as expressed in Eq. 17. This encoding significantly enhances the boundary between two classes as presented in Fig. 5c.

$$I_{global} = \left\{ Pr^{smth}(\mathbf{x} \in c_{k1}) - Pr^{smth}(\mathbf{x} \in c_{k2}) \right\}^2 \tag{17}$$

By substituting the two imaged based forces in Eq. 13, we obtain the hybrid curve driving force as expressed in Eq. 18.

$$F_{hybrid} = \delta\phi(\mathbf{x}) \int_{\Omega_{\mathbf{y}}} \phi(\mathbf{y}) B(\mathbf{x}, \mathbf{y}) \left\{ (I(\mathbf{y}) - c_1)^2 - (I(\mathbf{y}) - c_2)^2 + \beta I_{global}(\mathbf{y}) \right\} d\mathbf{y} \tag{18}$$

Based on the fact that the seed containing axial slice lies in the mid of the CTA volume, the initial mask is evolved in both directions along the caudo-cranial axis to capture the complete coronary tree. Generally, the coronary tree splits into branches as we move away from the aorta along the patient axis in the CTA volume. However, in some complex cases, the coronary peripheries emerge away from the main progression and join the tree as slices are navigated. To capture the potential side branches which emerge far from the main progression, we incorporated an auto-correction feature. The auto-correction feature captures the emerging peripheries during the curve evolution by scanning the neighbourhood of the main progression. This self-adjustment feature of the mask offers computational robustness without increasing processing load in terms of 3D level set segmentation. The non-connected components (based on false positive seed points or the auto-correction) are discarded in the final step with the help of morphological operations. Readers are referred to [35] for a detailed implementation of bidirectional evolution and auto-correction feature.

5. Results

We designed a Matlab based framework to compare the obtained segmentation with respect to the manual ground truth. For individual contours of the ground truth lumen, we computed the plane normal (perpendicular to the segment centreline) in the first stage. In the subsequent stage, we extracted the corresponding orthogonal planes from the segmented tree and the lumen boundary contours are identified as shown in Fig. 6a. The first stage of the quantification process is illustrated in Fig. 6b, where 3D segmented contours are plotted against manual ground truth. Next, we projected the 3D contours on a 2D plane where two polygons are interpreted as binary images as shown in Fig. 6c. In the final stage, we employed the Jaccard index to compute the overlap between two polygons.

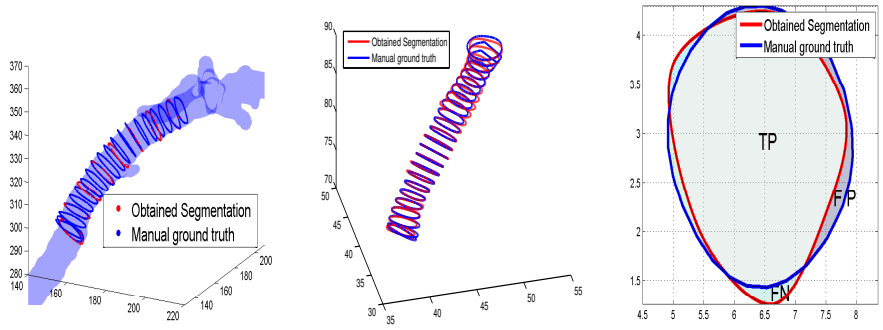

(a) 3D Coronary surface. (b) 3D contours. (c) Jaccard overlap.

Figure 6: Segmentation evaluation against manual ground truth of Rotterdam data. (a) shows the ground truth and the obtained segmentation contours overlaid on 3D coronary surface in voxel coordinate system. (b) presents a visual comparison of obtained segmentation with ground truth in world coordinate system, whereas (c) shows the Jaccard overlap computation for corresponding 2D contours based on TP, TN and FN.

The mathematical relation to obtain the Jaccard index between manual ground truth and the segmented image is as follows:

$$Jaccardindex = \frac{TP}{(TP + FP + FN)} \tag{19}$$

where TP denotes the true positive i.e. an intersection between two images, FP represents the false positive i.e. part of segmented image not present in the ground truth and FN denotes the false negative i.e. part of the ground truth missed in the obtained segmentation. The Jaccard index for overlapping segmentation approaches to one, whereas two dissimilar images results in Jaccard score of *zero*.

5.1. Analysis of 2D Images

As demonstrated in Fig. 4, the localization model successfully detect objects of interest when the initialization is fairly close to the object boundary, whereas it fails to handle perturbations because of the local optima problem. This shortcoming is further highlighted in Figs. 7 - 8 to illustrate the effectiveness of the proposed method over the localization model of [18] for 2D images (synthetic and clinical CPR respectively). It should be noted that the localization model is trapped in local optima leading to erroneous segmentation for different initializations, whereas the hybrid method results in successful segmentation for different initializations. Moreover, the weight regulating the influence of the global term can be adjusted to obtain a desired segmentation according to the nature of data or the initialization.

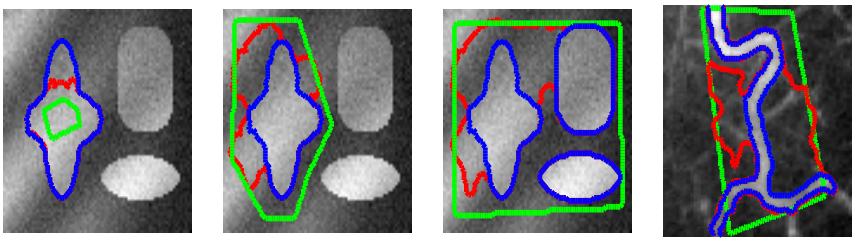

(a) $\beta = -0.53$ (b) $\beta = 0.20$ (c) $\beta = 0.65$ (d) $\beta = 0.35$

Figure 7: Performance of two segmentation methods for synthetic images. Blue and red show the hybrid and localization segmentation respectively, whereas green represents the initializations. The localization radius used for these results is 8 pixels.

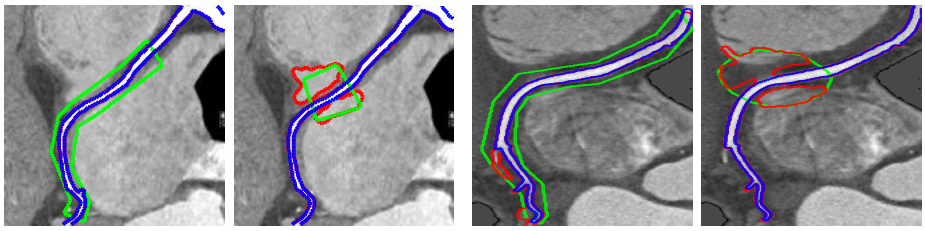

(a) $\beta = 0.1$ (b) $\beta = 0.7$ (c) $\beta = 0.1$ (d) $\beta = 0.8$

Figure 8: Performance of two segmentation methods for clinical images. (a) and (b) show right coronary of CTA volume 01 for two different initialization. (c) and (d) show right coronary of CTA volume 02 for two different initializations. Green denotes the initialization, whereas blue and red represents the hybrid and localized segmentation respectively. The localization radius used for these results is 8 pixels.

We also investigated the robustness of proposed model against the localization radius. Figs. 9 - 10 shows the response of the two methods when localization radius is decreased from 8 to 4 pixels.

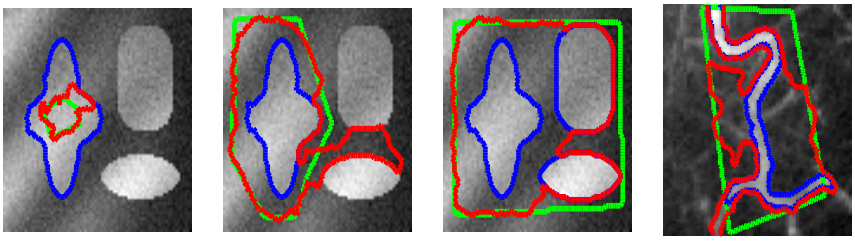

(a) $\beta = -0.83$ (b) $\beta = 0.45$ (c) $\beta = 0.82$ (d) $\beta = 0.75$

Figure 9: Performance of two segmentation methods for synthetic images. Blue and red show the hybrid and localization segmentation respectively, whereas green represents the initialization. The localization radius used for these results is 4 pixels.

325 It is evident that change in the radius degrades the performance of the localized model leading to incorrect segmentation, whereas the proposed model successfully delineates the object for the updated radius. We observed that there exists an inverse relationship between localization radius and the global weight

β. The smaller radius results in less information for the energy optimization process requiring more influence of the global term, whereas a large radius offers adequate intensity information, hence; less stimulus from the global term is required. This correlation is to be investigated in a future study to make the weight β adaptive against the localization radius and to define an image based threshold for the localization radius, as a very large radius leads to a global approximation of image which is not suitable for medical data.

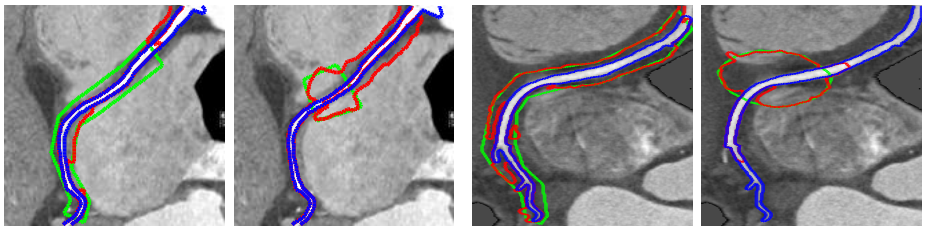

(a) $\beta = 0.3$ (b) $\beta = 0.78$ (c) $\beta = 0.24$ (d) $\beta = 0.91$

Figure 10: Performance of two segmentation methods for clinical images. (a) and (b) show right coronary of CTA volume 01 for two different initialization. (c) and (d) show right coronary of CTA volume 02 for two different initialization. Green denotes the initialization, whereas blue and red represents the hybrid and localized segmentation respectively. The localization radius used for these results is 4 pixels.

5.2. Analysis of 3D images

It becomes challenging to visually evaluate the segmentation quality in 3D space due to viewing angle limitations as shown in Fig. 11a. Thus, we extracted 2D slices orthogonal to the segment centreline at different points across the length of vessel to illustrate the effectiveness of the hybrid energy model over the localization method. Consequently, the lumen boundary based on orthogonal cross sections is compared with the ground truth contour as illustrated in Fig. 12. It is apparent from the figure that the curve moving under the influence of localized energy (blue) gets trapped away from the real lumen, whereas the integration of the global force pushes the contour further to attain a more accurate approximation (green). The explicit push of the contour towards the

lumen reduces the false positives and leads to an improved accuracy of the segmentation.

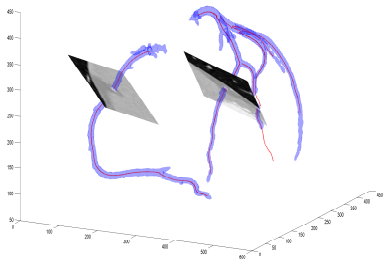

(a) 3D coronary surface, the centreline and oblique planes interpolated in 3D volume

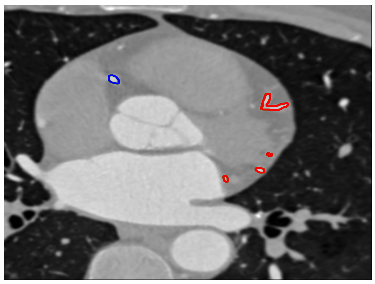

(b) An axial plane from CTA with overlaid segmentation

Figure 11: Coronary segmentation visualization. (a) shows the segmented 3D coronary tree with overlaid centreline and two oblique cross sections. (b) shows a 2D axial slice from CTA with the coronary segments outlined in two colours. Red shows the left coronary artery and blue represents the right coronary artery.

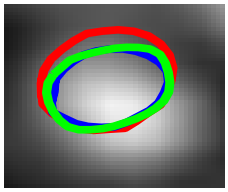

(a) Plane 4

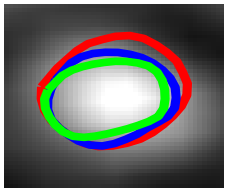

(b) Plane 6

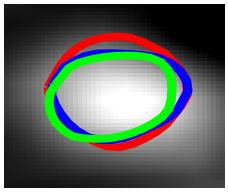

(c) Plane 8

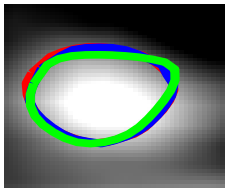

(d) Plane 10

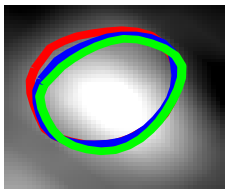

(e) Plane 12

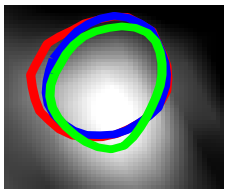

(f) Plane 14

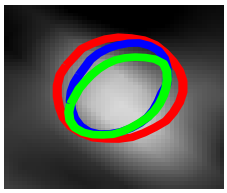

(g) Plane 16

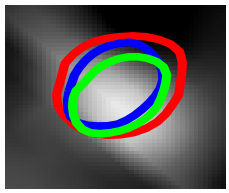

(h) Plane 18

Figure 12: Consecutive cross-sectional planes for segment-12 of CTA volume 01. Green is the expert's manual ground truth, blue represents the hybrid energy segmentation and red shows the segmentation for localized model [18].

Moreover, the statistical comparison of the two segmentation methods is presented in Fig. 13, where we plotted the respective false positive rate and the Jaccard index with respect to the ground truth annotations for two representative volumes. It should be noted that the mean results for complete Rotterdam dataset are presented in Table 2. To avoid biasing towards a particular expert, we compared the response of the two methods with three manual observers individually and it can be observed that the hybrid model consistently achieves higher Jaccard index in comparison to localization method of [18].

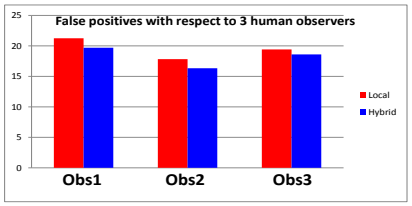

(a) CTA volume 10, False positive (%)

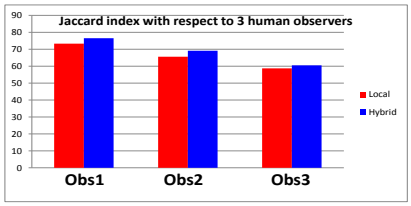

(b) CTA volume 10, Jaccard index (%)

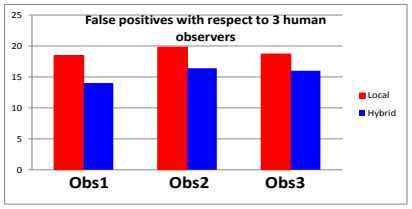

(c) CTA volume 13, False positive (%)

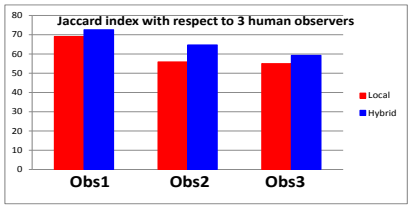

(d) CTA volume 13, Jaccard index (%)

Figure 13: Segmentation accuracy of two method with respect to three individual observers of Rotterdam Data. Low FP % and high Jaccard index consistently shows the advantage of hybrid model over the localization [18]. method

5.3. Evaluation based on Segment Classes

Before comparing the mean performance of the two segmentation methods for the complete Rotterdam dataset, we evaluated the hybrid segmentation in

a clinical context. From a clinical point of view, the coronary segments are divided into two classes namely major and minor segments. The major class refers to proximal sections close to the descending aorta, whereas the minor class refers to distal segments of the coronary tree. Any abnormality or occlusion in the major segments is treated as a severe clinical threat as the dependent branches are simultaneously affected resulting in considerable loss to the heart tissues. In contrast, the abnormality associated with the minor segments are less threatening as these segments does not affect other segments in parallel. Fig. 14a shows the mean performance of the hybrid energy model for complete Rotterdam data in context of these two classes.

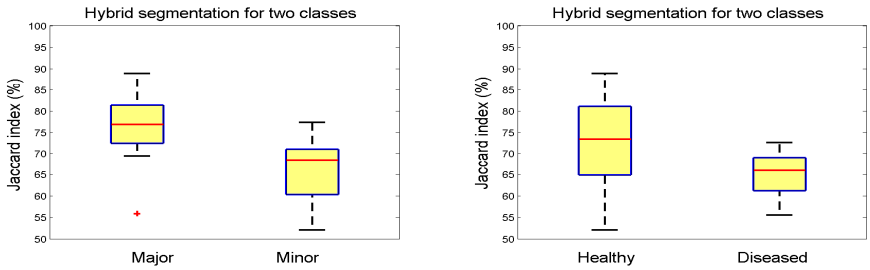

(a) Hybrid segmentation statistics for major - minor segments.

(b) Hybrid segmentation statistics for healthy - diseased segments.

Figure 14: The mean performance of the hybrid model for complete Rotterdam CTA data in a clinical context. (a) shows higher accuracy for major segments in comparison to minor branches, (b) shows higher accuracy for healthy segments in comparison to diseased branches.

The box plot is used based on the fact that distributional characteristics of different groups can be compared effectively. The high median value and the compact distribution reflects that the overall accuracy is fairly high and consistent for major segments, whereas the reduced diffusion, poor contrast and narrower diameter in minor segments results in reduced accuracy and high variability. Similarly, Fig. 14b shows the performance of the hybrid energy model using "healthy versus diseased" criteria. It should be noted that the segmentation accuracy for the healthy segments is high in comparison to the diseased

segments. The variability observed for the healthy class is unexpected, however this can be related with the immature plaques / lesion present in different segments. As the ground truth classification (healthy versus diseased) is done on the basis of visual inspection of the coronary tree, so there is a chance that segments with insignificant abnormalities were placed in healthy class; however, it effects the segmentation accuracy. On the other hand, the performance for the diseased class is persistent as this class contain significantly abnormal segments. To conclude, these results reveal the fact that it becomes difficult to precisely delineate the diseased segments, specially in the presence of low intensity based soft plaques. Moreover, the type and the progress of the abnormality directly affects the segmentation quality.

The relationship between the segmentation accuracy and "segment-class" is further investigated as shown in Fig. 15. The first row shows mutual agreement of three human experts for two representative coronary segments, whereas the second row presents the Jaccard index of two segmentation methods. It should be observed from Fig. 15a that the high concentration of the contrast medium in the proximal segment of the coronary tree leads to a good inter-observer agreement. Consequently, both segmentation models achieve an adequate quality segmentation and the Jaccard index shows a marginal superiority of hybrid model over the localization method in Fig. 15c. In contrast, lower concentration of the contrast medium results in the ambiguous appearance of distal segments, which leads to a significant inter-observer disagreement as shown in Fig. 15b. This results in an increased false positive ratio for the localization model, whereas the hybrid energy moderates false positives due to influence of global term in curve evolution (see Fig. 12). Consequently, the hybrid model shows a considerable improvement in the Jaccard index as plotted in Fig. 15d.

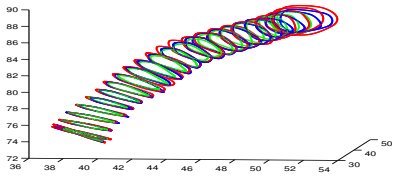

(a) CTA volume 01, segment 1, good inter-observer agreement

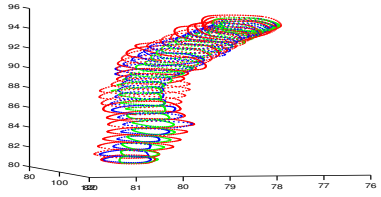

(b) CTA volume 01, segment 12, poor inter-observer agreement

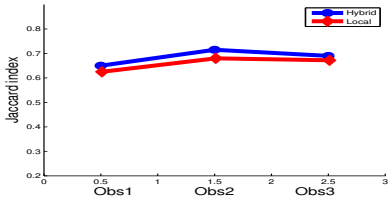

(c) Jaccard index for two methods in proximal segment

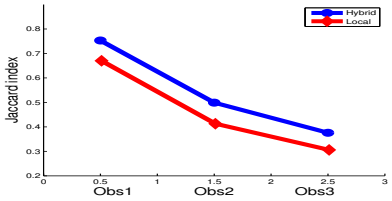

(d) Jaccard index for two methods in distal segment

Figure 15: Performance of two segmentation methods for different segment types. Good agreement among three manual observers (a) reflects the bright appearance of proximal segments. (b) the reduced agreement among three human observers due to the ambiguous appearance of distal segments. (c) and (d) represents the Jaccard index for two segmentation methods w.r.t three individual observers.

The comparative performance of two segmentation methods for complete Rotterdam dataset is presented in Table 2. The Jaccard index (with respect to

Table 2: Jaccard index (%) of two segmentation methods for Rotterdam CTA data.

Segment type	Jaccard index value	
	Local	Hybrid
Major	73.48	76.5
Minor	58.26	68.65
Healthy	68.21	71.62
Diseased	57.79	65.56

405

the manual annotations) shows that the hybrid energy achieves better segmentation over the localization model of [18] for all types of coronary segments. A considerable difference for the minor segments is related with the reduced false positive (%) due to the increased push of global term in hybrid segmentation, whereas lower Jaccard index value for the diseased segments reflect the complexity of segmentation. To validate the statistical significance of the hybrid energy model, we performed a paired $t-$test by employing results of two segmentation methods. Accordingly, the null hypothesis is rejected which indicates a significant difference in the mean of the two distributions. Moreover, we obtained p values equal to 0.0014 for the false positive rate and 0.0001 for the Jaccard index which indicates a statistically significant difference.

5.4. Comparison with Existing Coronary Segmentation Model

After validating the superiority of hybrid energy over [18], we compared the performance of the hybrid model with the coronary segmentation algorithm of Yang *et al.* [21], which implements an edge based conformal factor in the curve evolution. Fig. 16 - Fig. 17 demonstrates the efficacy of hybrid energy model over [21] with respect to the manual annotations. For comparative purpose, we start with the assumption that observer 1 of Rotterdam CTA data is the typical ground truth representing the "true" lumen. Segmentation statistics (sensitivity, specificity and Jaccard index) with respect to the observer 1 are presented in Fig. 16, whereas Fig. 17 shows the performance of two methods against mean human agreement of three observers. It can be observed from Fig. 16a that the higher true positive rate of the hybrid energy model leads to a higher sensitivity for all investigated volumes. Likewise, the reduced false positive rate results in comparatively better specificity for the hybrid model; however, a lower scale of specificity percent refers the fact that both methods found difficult to delineate the diseased segments. For the overall Jaccard overlapping index, it should be noted from Fig. 16c that the hybrid method outperforms the [21] model with a consistent higher index value.

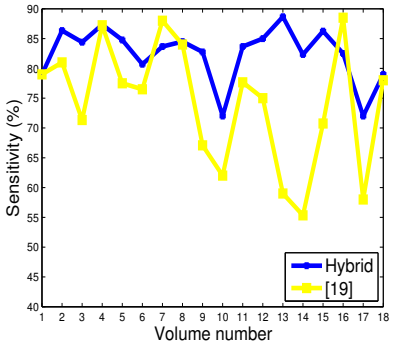

(a) Sensitivity with respect to observer 1 for complete CTA dataset.

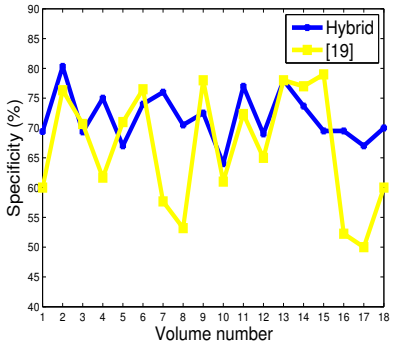

(b) Specificity with respect to observer 1 for complete CTA dataset.

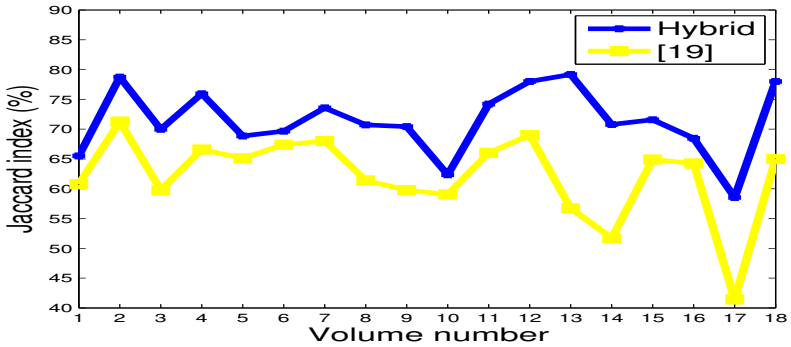

(c) Jaccard index with respect to observer 1 for complete CTA dataset.

Figure 16: Segmentation result for [21] and the hybrid segmentation method with respect to observer 1 of the Rotterdam data, (complete CTA dataset).

Fig. 17 shows the overall segmentation performance of two method in context of the mean human agreement of 3 human observers. It can be observed from the plot that the overall Jaccard index is dropped due to averaging against three manual annotations; however, the comparative performance of the proposed model remains superior to [21] model and shows a consistent bound with inter-observer mean agreement.

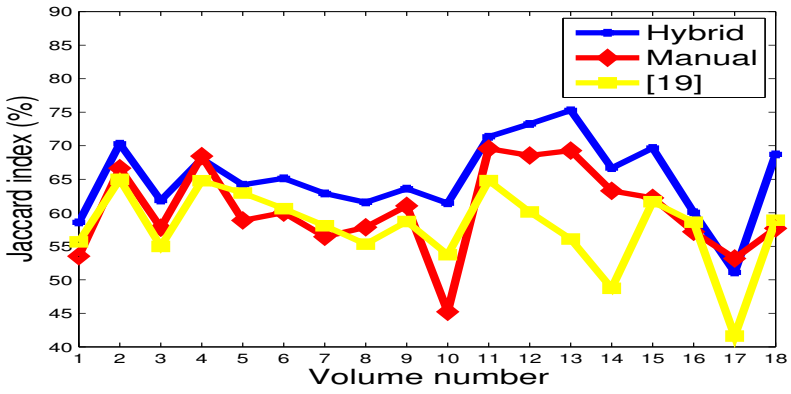

Figure 17: Segmentation result for the mean human agreement, [21] and the proposed method with respect to average of 3 observers, (complete CTA dataset).

It can be observed from the plot of Fig. 17 that there occurs a considerable dip in Jaccard index value for CTA datasets 10 and 17 (for all three segmentation methods). This unexpected drop is related with the structural abnormalities of the coronary tree as shown in Fig. 18a. These aberrations in coronary tree makes segmentation challenging even for the manual observers, as Fig. 18b shows a minimal agreement among three human experts.

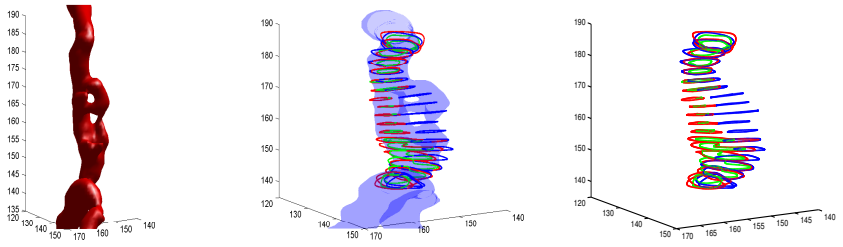

(a) (b) (c)

Figure 18: Illustration of the inconsistencies between manual observers. (a) A coronary structure with an aberration, which complicates segmentation. (b) Clinical annotations for lumen boundary for three observers (red, blue and green circles). (c) Magnification of the boundaries. Notice the inconsistent decision of the observers whilst delineating the lumen.

6. Discussion

A limitation of the proposed method is the manual selection of the appropriate weight β for the global term, as the true boundary is surpassed occasionally due to high influence of the global force. Subsequently, in the CTA volume based analysis, we evaluated different values for β from the normalized range [0, 0.01, 0.05, 0.10, 0.15, 0.25, 0.50, 0.75, 1.0] to derive an empirical evidence for best global weight. According to a series of experiment, the segmentation obtained with β less than 0.1 produces results similar to localization model of [18] due to very less influence of global term, whereas setting β greater than 0.25 results in suppression of distal segments due to very high influence of global term. This makes $\beta = 0.15, 0.25$ a feasible choice for effective segmentation of the coronary tree.

A primary drawback associated with the level set evolution is the processing time as the curve evolution in a higher space requires a large number of computations. However, the key to minimize the processing time is to exploit the fact that the curve changes position smoothly and does not hold abrupt jumps or discontinuities. Consequently, the area around the evolving curve is to be evaluated for new position i.e. only a narrow band is to be investigated. For a fair processing time, we employed the sparse field method of Whitaker [36] to evolve the curve as it promises the accurate but minimal representation of the evolving curve. Accordingly, the average time for segmentation of coronary vasculature on Matlab R2014 based Intel 3.4 GHz machine is 80 seconds.

It should be noted that the fully automatic segmentation of the coronary tree has been a challenging problem so far and the current research is focused to minimize the human interaction. Several methods [37, 38, 39, 40, 41] have been proposed in recent years addressing the automatic and semi-automatic segmentation of coronary lumen with a motivation of stenosis detection; however, a little attention has been paid on the negative remodelling of coronary vessels. From a clinical point of view, negative remodelling signals the presence of soft plaques which have been reported as most important indicator of heart attack

and stroke [42]. In context of the broader theme of our study, we compared our results with [21] method as the proposed idea of bidirectional evolution grabs effectively the negative remodelled vessels.

In future work, we aim to make the global weight β adaptive with respect to the localization radii for the robust automated implementation of the algorithm. Furthermore, we plan to use the segmented coronary tree in machine learning framework for the detection and localization of the non-calcified plaques as the future coronary segmentation research is to be steered by soft plaques quantification.

7. Conclusion

In this paper, we proposed a simple yet efficient segmentation method and demonstrated its efficacy for 3D coronary segmentation. An image discontinuity model is combined with a localized active contour segmentation which achieves better overlap with manual annotations. The proposed method is less sensitive to the local optima problem which helps in reducing false positives as well as it allows a certain degree of freedom for initialization. The capability to address the variations in initial mask and localization radii simultaneously, makes our algorithm a feasible choice for the coronary segmentation.

References

[1] S. Waxman, F. Ishibashi, J. E. Muller, Global, regional, and national age-sex specific all-cause and cause-specific mortality for 240 causes of death, 1990-2013: a systematic analysis for the global burden of disease study 2013, Lancet 385 (9963) (2015) 117–171.

[2] U. K. NHS, Coronary Heart Disease, statistics for united kingdom, Available at `http://www.nhs.uk/Conditions/Coronary-heart-disease/Pages/Introduction.aspx`(2016/11/11).

[3] T. Flohr, B. Ohnesorge, Multi-slice ct technology, in: Multi-slice and Dual-source CT in Cardiac Imaging, Springer, 2007, pp. 41–69.

[4] T. F. Chan, L. A. Vese, Active contours without edges, IEEE Transactions on image processing 10 (2) (2001) 266–277.

[5] H. Lu, Y. Li, Y. Wang, S. Serikawa, B. Chen, J. Chang, Active contours model for image segmentation: A review, in: The 1st International Conference on Industrial Application Engineering 2013 (ICIAE2013), 2013.

[6] M. Kass, A. Witkin, D. Terzopoulos, Snakes: Active contour models, International journal of computer vision 1 (4) (1988) 321–331.

[7] V. Caselles, Geometric models for active contours, in: International Conference on Image Processing, Vol. 3, 1995, pp. 9–12.

[8] V. Caselles, R. Kimmel, G. Sapiro, Geodesic active contours, International journal of computer vision 22 (1) (1997) 61–79.

[9] S. Osher, R. Fedkiw, Level set methods and dynamic implicit surfaces, Vol. 153, Springer Science & Business Media, 2006.

[10] G. Zhu, S. Zhang, Q. Zeng, C. Wang, Boundary-based image segmentation using binary level set method, Optical Engineering 46 (5) (2007) 050501–050501.

[11] A. Yezzi, A. Tsai, A. Willsky, A fully global approach to image segmentation via coupled curve evolution equations, Journal of Visual Communication and Image Representation 13 (1) (2002) 195–216.

[12] J. Wang, Y. Cheng, C. Guo, Y. Wang, S. Tamura, Shape–intensity prior level set combining probabilistic atlas and probability map constrains for automatic liver segmentation from abdominal ct images, International journal of computer assisted radiology and surgery 11 (5) (2016) 817–826.

[13] L. Wang, C. Li, Q. Sun, D. Xia, C.-Y. Kao, Active contours driven by local and global intensity fitting energy with application to brain mr image

segmentation, Computerized Medical Imaging and Graphics 33 (7) (2009) 520–531.

[14] C. C. Reyes-Aldasoro, Retrospective shading correction algorithm based on signal envelope estimation, Electronics letters 45 (9) (2009) 454.

[15] T. Brox, D. Cremers, On the statistical interpretation of the piecewise smooth mumford-shah functional, in: International Conference on Scale Space and Variational Methods in Computer Vision, Springer, 2007, pp. 203–213.

[16] D. Mumford, J. Shah, Optimal approximations by piecewise smooth functions and associated variational problems, Communications on pure and applied mathematics 42 (5) (1989) 577–685.

[17] H. Xu, T. Liu, G. Wang, Hybrid geodesic region-based active contours for image segmentation, Computers & Electrical Engineering 40 (3) (2014) 858–869.

[18] S. Lankton, A. Tannenbaum, Localizing region-based active contours, IEEE transactions on image processing 17 (11) (2008) 2029–2039.

[19] S. Lankton, A. Stillman, P. Raggi, A. Tannenbaum, Soft plaque detection and automatic vessel segmentation, in: 12th International Conference on MICCAI, Springer Berlin Heidelberg, 2009, pp. 25–33.

[20] Y. Cheng, X. Hu, J. Wang, Y. Wang, S. Tamura, Accurate vessel segmentation with constrained b-snake, IEEE Transactions on Image Processing 24 (8) (2015) 2440–2455.

[21] Y. Yang, A. Tannenbaum, D. Giddens, A. Stillman, Automatic segmentation of coronary arteries using bayesian driven implicit surfaces, in: 4th IEEE International Symposium on Biomedical Imaging: From Nano to Macro, IEEE, 2007, pp. 189–192.

[22] Y. Wang, P. Liatsis, An automated method for segmentation of coronary arteries in coronary ct imaging, in: DESE, IEEE, 2010, pp. 12–16.

[23] D. Han, N.-T. Doan, H. Shim, B. Jeon, H. Lee, Y. Hong, H.-J. Chang, A fast seed detection using local geometrical feature for automatic tracking of coronary arteries in cta, Computer methods and programs in biomedicine 117 (2) (2014) 179–188.

[24] W. Theo, The Great Challenge, coronary artery stenoses detection and quantification evaluation framework (2016).
URL `http://www.http://coronary.bigr.nl/stenoses/`

[25] H. Kirisli, M. e. a. Schaap, Standardized evaluation framework for evaluating coronary artery stenosis detection, stenosis quantification and lumen segmentation algorithms in computed tomography angiography, Medical image analysis 17 (8) (2013) 859–876.

[26] W. G. Austen, J. Edwards, A reporting system on patients evaluated for coronary artery disease. report of the adhoc committee for grading of coronary artery disease, council on cardiovascular surgery, american heart association, Circulation 51 (4) (1975) 5–40.

[27] H. Lusic, M. W. Grinstaff, X-ray-computed tomography contrast agents, Chemical reviews 113 (3) (2012) 1641–1666.

[28] R. O. Duda, P. E. Hart, Use of the hough transformation to detect lines and curves in pictures, Communications of the ACM 15 (1) (1972) 11–15.

[29] A. F. Frangi, W. J. Niessen, K. L. Vincken, M. A. Viergever, Multiscale vessel enhancement filtering, in: International Conference on Medical Image Computing and Computer-Assisted Intervention, Springer, 1998, pp. 130–137.

[30] J. T. Dodge, B. G. Brown, E. L. Bolson, H. T. Dodge, Lumen diameter of normal human coronary arteries. influence of age, sex, anatomic variation,

and left ventricular hypertrophy or dilation., Circulation 86 (1) (1992) 232–246.

[31] I. G. Shukri, J. M. Hawas, S. H. Karim, I. K. M. Ali, Angiographic study of the normal coronary artery in patients attending ulaimani center for heart diseases, European Scientific Journal, ESJ 10 (24).

[32] C. Saikrishna, S. Talwar, G. Gulati, A. S. Kumar, Normal coronary artery dimensions in indians, Indian Journal of Thoracic and Cardiovascular Surgery 22 (3) (2006) 159–164.

[33] A. P. Dempster, N. M. Laird, D. B. Rubin, Maximum likelihood from incomplete data via the em algorithm, Journal of the royal statistical society. Series B (methodological) (1977) 1–38.

[34] P. Perona, J. Malik, Scale-space and edge detection using anisotropic diffusion, IEEE Transactions on pattern analysis and machine intelligence 12 (7) (1990) 629–639.

[35] M. M. Jawaid, Segmentation of soft atherosclerotic plaques using active contour models, arXiv preprint arXiv:1608.00116.

[36] R. T. Whitaker, A level-set approach to 3d reconstruction from range data, International journal of computer vision 29 (3) (1998) 203–231.

[37] R. Shahzad, Automatic segmentation, detection and quantification of coronary artery stenoses on cta, The international journal of cardiovascular imaging 29 (8) (2013) 1847–1859.

[38] Y. Kitamura, Y. Li, W. Ito, H. Ishikawa, Coronary lumen and plaque segmentation from cta using higher-order shape prior, in: MICCAI, Springer, 2014, pp. 339–347.

[39] F. Lugauer, Y. Zheng, J. Hornegger, B. M. Kelm, Precise lumen segmentation in coronary computed tomography angiography, in: MICCAI Workshop on Medical Computer Vision, Springer, 2014, pp. 137–147.

[40] B. Mohr, S. Masood, C. Plakas, Accurate lumen segmentation and stenosis detection and quantification in coronary cta, in: Proceedings of 3D Cardiovascular Imaging: a MICCAI segmentation challenge workshop, 2012.

[41] C. Feng, Y. Hu, Segmentation of coronary artery using region based level set with edge preservation, Journal of Medical Imaging and Health Informatics 6 (7) (2016) 1727–1731.

[42] R. Virmani, A. P. Burke, A. Farb, F. D. Kolodgie, Pathology of the vulnerable plaque, Journal of the American College of Cardiology 47 (81) (2006) C13–C18.